Electrically-driven phase transition in magnetite nanostructures

Sungbae Lee[1], Alexandra Fursina[2], John T. Mayo[2], Cafer T. Yavuz[2], Vicki L. Colvin[2], R. G. Sumesh Sofin[3], Igor V. Shvets[3], D. Natelson[1,4]

[1]*Department of Physics and Astronomy, Rice University, 6100 Main St., Houston, TX 77005*

[2]*Department of Chemistry, Rice University, 6100 Main St., Houston, TX 77005*

[3]*CRANN, School of Physics, Trinity College, Dublin 2, Ireland*

[4]*Department of Electrical and Computer Engineering, Rice University, 6100 Main St., Houston, TX 77005*

Magnetite (Fe_3O_4), an archetypal transition metal oxide, has been used for thousands of years, from lodestones in primitive compasses[1] to a candidate material for magnetoelectronic devices.[2] In 1939 Verwey[3] found that bulk magnetite undergoes a transition at $T_V \approx 120$ K from a high temperature "bad metal" conducting phase to a low-temperature insulating phase. He suggested[4] that high temperature conduction is via the fluctuating and correlated valences of the octahedral iron atoms, and that the transition is the onset of charge ordering upon cooling. The Verwey transition mechanism and the question of charge ordering remain highly controversial.[5–11] Here we show that magnetite nanocrystals and single-crystal thin films exhibit an electrically driven phase transition below the Verwey temperature. The signature of this transition is the onset of sharp conductance switching in high electric fields, hysteretic in voltage. We demonstrate that this transition is not due to local heating, but

instead is due to the breakdown of the correlated insulating state when driven out of equilibrium by electrical bias. We anticipate that further studies of this newly observed transition and its low-temperature conducting phase will shed light on how charge ordering and vibrational degrees of freedom determine the ground state of this important compound.

Strongly correlated electronic materials can exhibit dramatic electronic properties (*e.g.*, high temperature superconductivity, metal-insulator transitions, and charge ordering) not present in simple systems with weaker electron-electron interactions. Such rich electronic phenomenology can result when electron-electron interactions, electron-phonon interactions, and electronic bandwidth are all of similar magnitude, as in magnetite.[12] Verwey[3] found nearly seven decades ago that bulk magnetite, while moderately conductive at room temperature, undergoes a transition to a more insulating state below what is now called the Verwey temperature, $T_{\rm V} \approx 120$ K. Similar transitions are known in a number of materials.[13,14] Above $T_{\rm V}$, Fe_3O_4 has an inverse-spinel structure of the form AB_2O_4, with tetrahedrally coordinated A sites occupied by Fe^{3+} and octrahedrally coordinated B sites of mixed valence, equally occupied by irons with formal $+3$ and $+2$ charges. Conduction at high temperatures has long been thought to be through fluctuating valences of the B sites, with the transition corresponding to some kind of B site charge ordering as T decreases; concurrent is a first-order structural phase transition to an orthorhombic unit cell. This explanation remains controversial,[5,6] with experiments showing some charge disproportion or charge order (CO),[7,8] and others implying that the structural degrees of freedom drive the change in conductivity.[9,10] Recent theoretical progress has been made in understanding the complex interplay of charge and structural degrees of freedom[15,16], including a complete picture of the transition mechanism [11] with

strongly correlated $3d$ Fe electrons acting to amplify electron-phonon couplings. Testing these ideas experimentally is of much interest.

In this Letter we report electronic transport measurements in magnetite at the nanoscale on both nanocrystals and single-crystal epitaxial thin films. Both types of devices exhibit striking electrically-driven hysteretic switching of the electronic conductance once sample temperatures are reduced below $T_{\rm V}$. The data clearly show that the transition is not the result of local heating above $T_{\rm V}$, but instead is an electrically-driven breakdown of the insulating state. We discuss possible explanations for this switching in the context of the general Verwey transition problem. While qualitatively similar resistive switching has been observed in other correlated oxide systems[17,18], the phenomenon in Fe_3O_4 is a bulk effect with a mechanism distinct from these.

Two-terminal devices for applying voltages and measuring conduction at the nanoscale have been fabricated (see Methods) incorporating both Fe_3O_4 nanocrystals[19] (10-20 nm in diameter with oleic acid coating) and single-crystal thin films (40-60 nm thick).[20] Devices were measured in both a variable temperature vacuum probe station and a ^{4}He cryostat with magnet. Current-voltage characteristics have been measured with both a semiconductor parameter analyzer and directly using voltage sources and current amplifiers, with differential conductance computed numerically.

Figure 1a shows $I-V$ characteristics of a nanocrystal device at selected temperatures. When cooling, zero-bias conductance decreases monotonically until $T \rightarrow T_{\rm V}$. Below $T_{\rm V}$, the $I-V$ characteristics show sharp switching between a low bias insulating state and a high bias state with

much higher differential conductance $dI/dV(V)$ (close to $dI/dV(V = 0, T = 300\ \mathrm{K})$), with dramatic hysteresis as a function of voltage sweep direction. The switching threshold voltages increase in magnitude as T is decreased.

Dozens of nanocrystal devices were measured and only those with 300 K resistances below 10 kΩ showed the switching, with higher resistance devices having higher switching threshold voltages. Resistances decrease by some three orders of magnitude with vacuum annealing at 673 K, likely because of oleic acid decomposition.[21,22] The temperature dependence (Fig. 1a, inset) of the zero-bias resistance, $R(T)$, has no step at T_{V}, showing that $R(T)$ remains dominated by contact effects.

Qualitatively identical conduction is apparent in the thin film devices, as shown in Fig. 1b. Contact resistances are also important in these structures, as demonstrated by examining R at low bias (< 100 mV) as a function of channel length, L, as shown in the inset for one set of devices. Extrapolating back to $L \rightarrow 0$, the contact resistance, R_{c}, at 300 K is 390 Ω, while the 50 nm thick channel of width 20 μm contributes 27.2 Ω/micron, implying (based on channel geometry) a magnetite resistivity of 2.9 mΩ-cm, somewhat below bulk expectations. Further investigations are seeking to understand and minimize R_{c}. Analysis of $R(L)$ at lower temperatures shows that R_{c} increases significantly as T is decreased, exceeding 80 kΩ by 80 K. This complicates the analysis of the switching, since some of the total V is dropped across R_{c} rather than directly within the Fe_3O_4; further, the contacts may not be Ohmic near the switching threshold. We return to this

issue later.

The transitions in all devices are extremely sharp, with widths less than 50 μV, though in repeated sweeps at a fixed temperature, there is sweep-to-sweep variability of a few mV in switching thresholds. Using the substrate as a gate electrode, no discernable gate modulation was seen in nanocrystal devices for gate biases between -80 V and +80 V; this suggests that nanocrystal charging effects do not dominate. Switching characteristics were independent of magnetic field perpendicular to the sample surface up to 9 T, showing no large coupling between magnetization and the transition.

Differential conductance traces (Figure 2) show the transition even more dramatically. In the high conductance state, dI/dV is relatively temperature independent. As T is decreased, a clear zero-bias suppression develops, deepening into a hard gap when $T < T_{\rm V}$. In the nanocrystal data there are indications (in $d^2I/dV^2(V)$) of gap formation even at 150 K. We note that $T_{\rm V}$ in nanocrystals could be elevated, since nanocrystals have large surface-to-volume ratios and the transition temperature of the magnetite surface is known to be higher than in the bulk.[23]

Several lines of evidence indicate that these sharp conductance transitions are *not* the result of local Joule heating (as in macroscopic samples of Fe_3O_4 [24,25] and in the Mott insulator VO_2 [26,27]), but rather are electrically driven. In the worst-case scenario, all of the $I \times V$ Joule heating power is dissipated within the magnetite, and inhomogeneous dissipation (*e.g.*, filamentary conduction through a locally heated path) can complicate the analysis. The local steady-state temperature

is determined by the power dissipated and the thermal path. Thermally driven switching would then correspond to raising the *local* temperature above $T_{\rm V}$. At a fixed cryostat temperature an improved thermal path would imply that more power dissipation would be required for a given local temperature rise. Similarly, for a fixed thermal path, the necessary dissipated power for thermal switching would approach zero as $T \rightarrow T_{\rm V}$. Furthermore, at a given cryostat temperature thermally-driven switching would imply that the power dissipated at the low-to-high conductance transition (needed to raise the local temperature to $T_{\rm V}$) should be close to that at the high-to-low conductance transition.

The thermal conductivity, κ, of magnetite is dominated by phonons in this temperature range, and limited by phonon-electron scattering,[28] even when $T > T_{\rm V}$. As a result, κ increases as T is *decreased* through and below $T_{\rm V}$, and the material's thermal coupling to the cryostat *improves* as T is reduced. In *all* devices showing switching, the electrical power required to switch from low to high conductance *decreases* with decreasing T, with Fig. 3 showing one example. This is precisely the opposite of what one would expect from thermally-driven switching. Similarly, in all devices the power dissipated at switching does *not* approach zero as $T \rightarrow T_{\rm V}$, again inconsistent with thermally-driven switching. Furthermore, at a given T the power dissipated just before V is swept back down through the high-to-low conductance threshold significantly exceeds that dissipated at the low-to-high point in many devices, including those in Fig. 1, inconsistent with thermal switching expectations. Finally, nanocrystal and thin film devices show quantitatively similar switching properties and trends with temperature, despite what would be expected to be very different thermal paths. These switching characteristics are also qualitatively very different from

those in known inhomogeneous Joule heating.[24,25]. These facts rule out local heating through the Verwey transition as the cause of the conductance switching.

Figure 3 (inset) shows details of hysteresis loops on a nanocrystal device comparing different voltage sweep rates. The loop shape and switching voltages are unchanged to within the precision of the data collection as voltage sweep rates are varied from around 0.7 V/s up to 70 V/s. This indicates that the switching process is relatively rapid. Further studies will examine the intrinsic switching speed.

The observed conductance transition appears to be driven *electrically*. Figure 4 is a plot of the low-to-high conductance switching voltage as a function of L in a series of film devices for several temperatures. The linear dependence implies that the transition is driven by electric field itself, rather than by the absolute magnitude of the voltage or the current density. The fact that the voltage extrapolates to a nonzero value at $L = 0$ is likely a contact resistance effect. Minimizing and better understanding the contact resistance will allow the determination of the electric field distribution within the channel.

The length scaling of the transition voltage also demonstrates that this is a *bulk* effect. The contacts in all of these devices are identical, so any change in switching properties must result from the magnetite channel. This is in contrast to the resistive switching in $Pr_{0.7}Ca_{0.3}MnO_3$ (PCMO) that is ascribed to a change in contact resistance due to occupation of interfacial states[18].

The field-driven conductance transition may give insights into the equilibrium Verwey transition. This switching may be useful in testing recent calculations[11,15,16] about the role of strongly correlated B-site Fe $3d$ electrons and their coupling to phonons in the Verwey transition mechanism. It is interesting to ask, to what degree is the field-driven electronic transition coupled to the local structure? It is greatly desirable to perform local probes of the magnetite structure (via x-ray or electron-diffraction techniques or scanned probe microscopy) *in situ* in the channel of biased devices, to see if the coherence between structural symmetry changes and the formation of a gap in the electronic spectrum is broken under these noequilibrium conditions. This is a significant experimental challenge. Similarly, local Raman spectroscopy of devices under bias could reveal field-induced changes in phonon modes and electron-phonon couplings, and single-crystal thin films permit the application of bias along well-defined crystallographic directions relevant to structural symmetry changes at $T_{\rm V}$. We do note that qualitatively identical switching occurs in nanocrystal devices as in strained thin films strongly coupled to rigid MgO substrates. This suggests that elastic constraints on scales much larger than the unit cell have relatively little influence on the observed switching.

It is also possible that the nonequilibrium carrier distribution contributes to destabilizing the insulating state. In the presence of a strong electric field a carrier can gain significant energy even in a *single* hopping step, even though carrier relaxation times are very short. A rough estimate of the average critical E-field for switching at 80 K is 10^7 V/m, from the slope of the line in Fig. 4. The high temperature cubic unit cell is 0.84 nm on a side, meaning that a carrier traversing one cell would gain approximately 8.4 meV, comparable to $k_{\rm B}T_{\rm V} \approx 10.3$ meV. Conductance switching at

such high fields may require consideration of such nonequilibrium carrier dynamics.

The presence of multiple switching transitions in individual nanocrystal and film devices also bears further study. The suggested charge order may melt inhomogeneously, with portions of the channel having different switching thresholds. There could also be charge-ordered intermediate states between the insulating regime and the most conducting regime.[5] Again, optical measurements[12] with sufficient spatial resolution could address these possibilities. Through improved metal/magnetite contacts and further study, it should be possible to unravel the precise nature of this nonequilibrium transition, and its relationship to the equilibrium, bulk Verwey transition.

Methods

Magnetite nanocrystals were prepared via solution-phase decomposition of iron carboxylate salts.[19] The nanocrystals have been characterized by transmission electron microscopy (TEM), x-ray diffraction, and infrared and Raman spectroscopy, as discussed in Supplemental Material. As synthesized the nanocrystals are protected by weakly bound oleic acid ligands; these ligands allow the suspension of the nanocrystals in organic solvents, but act as electrically insulating layers that must be largely removed for effective electronic transport measurements.

Two-step electron beam lithography and e-beam evaporation (1 nm Ti, 15 nm Au) were used to pattern closely spaced source and drain electrode pairs onto degenerately n-doped silicon substrates coated with 200 nm of thermally grown SiO_2. Interelectrode gaps (channel lengths)

ranged from zero to tens of nm, with a 10 μm wide channel region. Nanocrystals were spin-coated from hexane solutions to form slightly more than one densely packed monolayer of nanocrystals over the channel region. Samples were then baked at 673 K in vacuum for 1 hr to remove as much of the oleic acid as possible. In one set of samples, a second layer of particles was added followed by a second round of baking.

The other class of devices are based on epitaxial magnetite films 50 nm thick grown by oxygen-plasma-assisted molecular beam epitaxy (MBE) on $\langle 100 \rangle$ MgO single-crystal substrates. Details of the growth process have been reported elsewhere.[20] Single-step e-beam lithography and e-beam evaporation were used to pattern Au (no Ti adhesion layer) source and drain electrodes defining a channel length ranging from tens of nm to hundreds of nm, and a channel width of 20 μm. The interelectrode conduction is dominated by the channel region due to this geometry. No annealing was performed following electrode deposition.

1. Mills, A. A. The lodestone: history, physics, and formation. *Ann. Science* **61**, 273-319 (2004).

2. Coey, J. M. D. & Chien, C. L. Half-metallic ferromagnetic oxides. *MRS Bulletin* **28**, 720-724 (2003).

3. Verwey, E. J. W. Electronic conduction in magnetite (Fe_3O_4) and its transition point at low temperatures. *Nature* **144**, 327-328 (1939).

4. Verwey, E. J. W. & Haayman, P. W. Electronic conductivity and transition point of magnetite. *Physica* **8**, 979-987 (1941).

5. Walz, F. The Verwey transition - a topical review. *J. Phys.: Condens. Matter* **14**, R285-R340 (2002).

6. Garciá, J. & Subías, G. The Verwey transition - a new perspective. *J. Phys.:Condens. Matter* **16**, R145-R178 (2004).

7. Huang, D. L. *et al.* Charge-orbital ordering and Verwey transition in magnetite measured by resonant soft x-ray scattering. *Phys. Rev. Lett.* **96**, 096401 (2006).

8. Nazarenko, E. *et al.* Resonant x-ray diffraction studies on the charge ordering in magnetite. *Phys. Rev. Lett.* **97**, 056403 (2007).

9. Subías, G. *et al.* Magnetite, a model system for mixed-valence oxides, does not show charge ordering. *Phys. Rev. Lett.* **93**, 156408 (2004).

10. Rozenberg, G. K. *et al.* Origin of the Verwey transition in magnetite. *Phys. Rev. Lett.* **96**, 045705 (2006).

11. Piekarz, P., Parlinksi, K. & Oleś, A. M. Mechanism of the Verwey transition in magnetite. *Phys. Rev. Lett.* **97**, 156402 (2006).

12. Gasparov, L. V. *et al.* Infrared and Raman studies of the Verwey transition in magnetite. *Phys. Rev. B* **62**, 7939-7944 (2000).

13. Imada, M., Fujimori, A. & Tokura, Y. Metal-insulator transitions. *Rev. Mod. Phys.* **70**, 1039-1263 (1998).

14. Coey, M. Condensed-matter physics: Charge-ordering in oxides. *Nature* **430**, 155-157 (2004).

15. Leonov, I., Yaresko, A. N., Antonov, V. N. & Anisimov, V. I. Electronic structure of charge-ordered Fe_3O_4 from calculated optical, magneto-optical Kerr effect, and O K-edge x-ray absorption spectra. *Phys. Rev. B* **74**, 165117 (2006).

16. Pinto, H. P. & Elliot, S. D. Mechanism of the Verwey transition in magnetite: Jahn-Teller distortion and charge ordering patterns. J. Phys.: Condens. Matter **18**, 10427-10436 (2006).

17. Asamitsu, A., Tomioka, Y., Kuwahara, H. & Tokura, Y. Current switching of ressitive states in magnetoresistive manganites. Nature **388**, 50-52 (1997).

18. Sawa, A., Fujii, T., Kawasaki, M. & Tokura, Y. Hysteretic current-voltage characteristics and resistance switching at a rectifying Ti/$Pr_{0.7}Ca_{0.3}MnO_3$ interface. Appl. Phys. Lett. **85**, 4073-4075 (2004).

19. Yu, W. W., Falkner, J. C., Yavuz, C. T. & Colvin, V. L. Synthesis of monodisperse iron oxide nanocrystals by thermal decomposition of iron carboxylate salts. *Chem. Commun.* **2004**, 2306-2307 (2004).

20. Zhou, Y., Jin, X. & Shvets, I. V. Enhancement of the magnetization saturation in magnetite (100) epitaxial films by thermo-chemical treatment. *J. Appl. Phys.* **95**, 7357-7359 (2004).

21. Pérez-Diete, V. *et al.* Thermal decomposition of surfactant coatings on Co and Ni nanocrystals. *Appl. Phys. Lett.* **83**, 5053-5055 (2003).

22. Zeng, H. *et al.* Magnetotransport of magnetite nanoparticle arrays. *Phys. Rev. B* **73**, 020402(R) (2006).

23. Shvets, I. V. *et al.* Long-range charge order on the $Fe_3O_4(001)$ surface. *Phys. Rev. B* **70**, 155406 (2004).

24. Burch, T. *et al.* Switching in magnetite: a thermally driven magnetic phase transition. *Phys. Rev. Lett.* **23**, 1444-1447 (1969).

25. Freud, P. J. & Hed, A. Z. Dynamics of the electric-field-induced conductivity transition in magnetite. *Phys. Rev. Lett.* **23**, 1440-1443 (1969).

26. Duchene, J., Terraillon, M., Pailly, P. & Adam, G. Filamentary conduction in VO2 coplanar thin-film devices. *Appl. Phys. Lett.* **19**, 115-117 (1971).

27. Gu, Q., Falk, A., Wu, J., Ouyang, L. & Park, H. Current-driven phase oscillation and domain-wall propagation in $W_xV_{1-x}O_2$ nanobeams. *Nano Lett.* **7**, 363-366 (2007).

28. Salazar, A., Oleaga, A., Wiechec, A., Tarnawski, Z. & Kozlowski, A. Thermal diffusivity of $Fe_{3-x}Zn_xO_4$. *IEEE Trans. Magn.* **40**, 2820-2822 (2007).

Supplementary Information is linked to the online version of the paper at www.nature.com/nature.

Acknowledgements This work was supported by the US Department of Energy grant DE-FG02-06ER46337. DN also acknowledges the David and Lucille Packard Foundation and the Research Corporation. VLC acknowledges the NSF Center for Biological and Environmental Nanotechnology (EEC-0647452), Office of Naval Research (N00014-04-1-0003), and the US Environmental Protection Agency Star Program (RD-83253601-0). CTY acknowledges a Robert A. Welch Foundation (C-1349) graduate fellowship. RGSS and IVS acknowledge the Science Foundation Ireland grant 06/IN.1/I91.

Author Contributions SL fabricated and measured the devices in this work and analyzed the data. AF fabricated devices and performed XRD characterization of the nanocrystal materials. DN and SL wrote the paper. JTM and CYZ made the nanocrystals in VLC's laboratory, and VLC contributed expertise in nanomaterials chemistry and characterization. RGSS and IVS grew the magnetite films, and IVS contributed expertise on magnetite physical properties. All authors discussed the results and commented on the manuscript.

Competing Interests The authors declare that they have no competing financial interests.

Correspondence Correspondence and requests for materials should be addressed to D.N. (email: natelson@rice.edu).

Figure 1 Hysteretic conductance switching below $T_{\rm V}$. (a) Current-voltage characteristics at various temperatures for a device based on 10 nm magnetite nanocrystals. Arrows indicate the direction of the hysteresis. Inset: Zero-bias resistance, $R(T)$. (b) Analogous data for a device based on a 50 nm-thick MBE-grown magnetite film. The nominal interelectrode gap was planned to be 100 nm, but at its narrowest was approximately 10 nm. Inset: Two-terminal resistance as function of channel length for another set of devices fabricated on another piece of the same film.

Figure 2 Differential conductance plots of the switching. (a) dI/dV vs. V for the nanocrystal device from Fig. 1a at the same temperatures. (b) dI/dV vs. V for the thin film device from Fig. 1b. Both plots have logarithmic dI/dV axes to better show the lowest temperature data.

Figure 3 Power required to switch from the insulating into the more conducting state as a function of temperature, for a device based on $\sim$20 nm diameter nanocrystals. Inset: Hysteresis loop in the conduction of the same device at 80 K, showing essentially no change in switching characteristics as the voltage sweep rate is varied over two orders of magnitude.

Figure 4 Switching voltages in a series of film devices as a function of channel length at several temperatures. The linear variation with L strongly implies that for each temperature there is a characteristic electric field required for switching. The non-zero intercepts of the trend lines indicate that some device-dependent threshold voltage must be exceeded for switching even when $L = 0$, suggestive of contact effects.

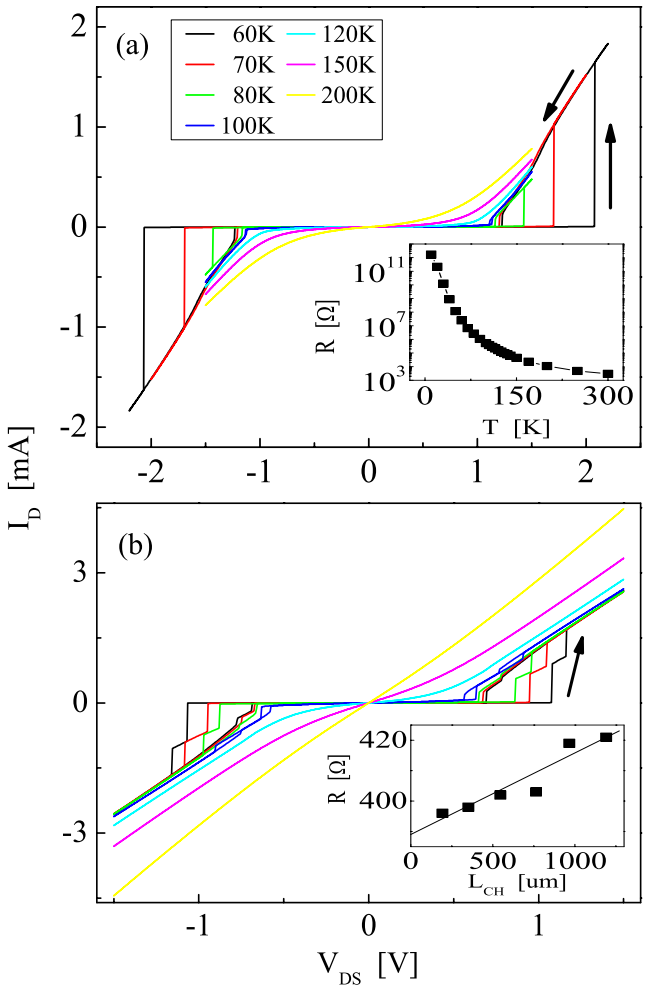
(a)
60K
70K
80K
100K
120K
150K
200K
R [Ω]
T [K]
(b)
R [Ω]
L_CH [um]
I_D [mA]
V_DS [V]

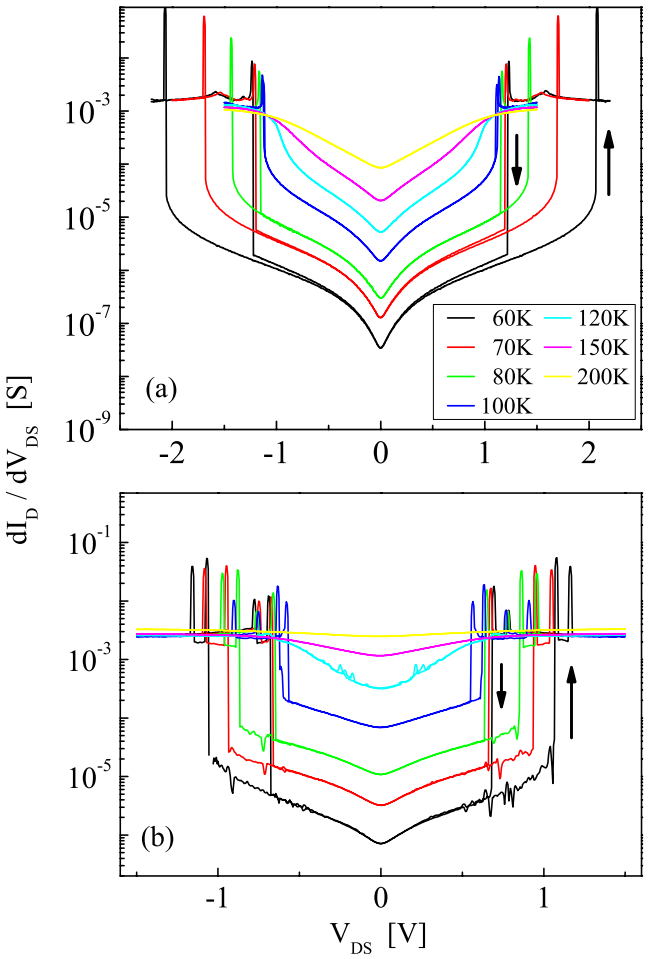
10^-3
10^-5
10^-7
10^-9
-2
-1
0
1
2
60K
70K
80K
100K
120K
150K
200K
(a)
10^-1
10^-3
10^-5
-1
0
1
(b)
dI_D / dV_DS [S]
V_DS [V]

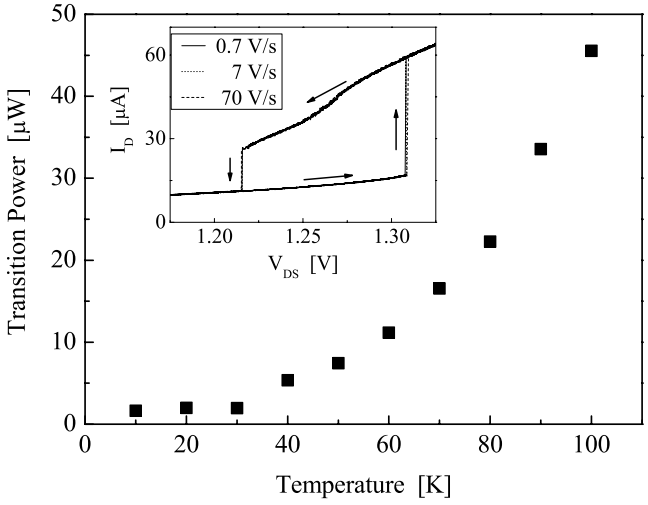
Transition Power [μW]
Temperature [K]
0
10
20
30
40
50
0
20
40
60
80
100
0.7 V/s
7 V/s
70 V/s
I_D [μA]
V_{DS} [V]
0
30
60
1.20
1.25
1.30

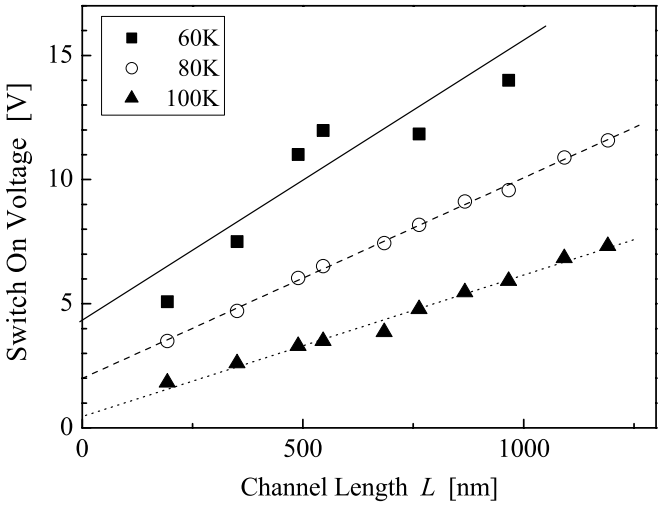
60K
80K
100K
Switch On Voltage [V]
Channel Length L [nm]
0
5
10
15
0
500
1000

Supplementary Information: Electrically-driven phase transition in magnetite nanostructures

Sungbae Lee[1], Alexandra Fursina[2], John T. Mayo[2], Cafer T .Yavuz[2], Vicki L. Colvin[2], R. G. Sumesh Sofin[3], Igor V. Shvets[3], Douglas Natelson[1, 4]

[1]Department of Physics and Astronomy, Rice University, Houston, TX 77251, USA; [2]Department of Chemistry, Rice University, Houston, TX 77251, USA; [3]CRANN, School of Physics, Trinity College, Dublin 2, Ireland; [4]Department of Electrical and Computer Engineering, Rice University, Houston, TX 77251, USA

Magnetite film sample preparation

The Fe_3O_4 thin films (50nm) used in the present study were grown on (100) oriented MgO single crystal substrates (cut along <100> direction within ±0.5^o) using oxygen plasma assisted molecular beam epitaxy, MBE, system (DCA MBE M600) with a base pressure $2x10^{-10}$ Torr. The substrates were cleaned in-situ at 600^o C in $5x10^{-6}$ Torr oxygen for two hours. Growth of the Fe_3O_4 films was carried out at a substrate temperature of 250^{o}C from a pure metallic Fe source by means of electron beam evaporation and oxygen free radicals generated by the electron cyclotron resonance (ECR) plasma source. The plasma source was operated at 80 W power in an oxygen partial pressure of $1x10^{-5}$ Torr. Reflection high energy electron diffraction, RHEED, (STAIB Instruments) was used to monitor the growth mode and growth rate (0.3 Å/s).

Magnetisation measurement of films

Magnetization measurements were performed using an alternating gradient field magnetometer (Micromag-3900, Princeton Measurements, USA) with a sensitivity of 10^{-8} emu. The magnetization verses field (M-H) loops were measured at room temperature by applying the magnetic field (maximum field of 1 Tesla) in the film plane along the <100> direction. The diamagnetic contribution from the MgO substrate was subtracted from the

measured data by performing a M-H loop of the MgO substrate of similar dimensions as that of thin film sample, in the same field range. The uncertainty in measuring the absolute value of magnetization for the films was about 1 %.

Supplementary Figure 1 shows the in-plane hysteresis loops measured at room temperature for a 50nm film. Saturation magnetization (M) values attained at 1 T field were found to be 475 emu/cm^3. These values are smaller than the saturation magnetisation value of bulk Fe_3O_4 (480emu/cm^3). Observation of reduced magnetization and finite slope seen at higher fields is indicative of the presence of areas with frustrated exchange. Observation of reduced M and inability to saturate epitaxial Fe_3O_4 films is attributed to the presence of APBs [1,2].

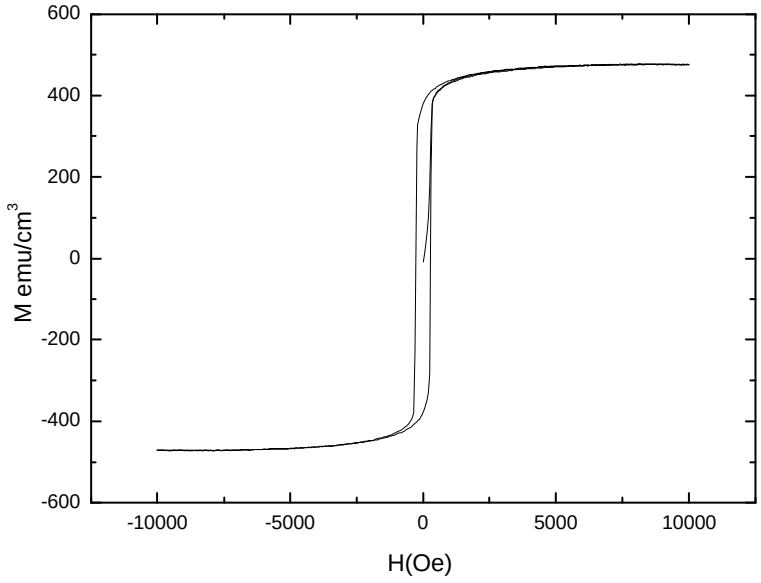

Supplementary Figure 1: Magnetization curve obtained for 50nm epitaxial magnetite film grown on MgO substrate.

Structural characterization of films

Structural characterization of Fe_3O_4 thin films was done using a multi-crystal high-resolution x-ray diffractometer, HRXRD (Bede-D1, Bede, UK).. The HRXRD in double or triple axis configuration was performed to confirm the epitaxial relationship of the Fe_3O_4/MgO and Fe_3O_4/$MgAl_2O_4$ hetero-epitaxy. The in-plane ($a_{||}$) and out-of-plane ($a_{\perp}$) lattice parameters were determined from the analysis of ω-2θ scans measured around the symmetric (200) and asymmetric (311) diffraction planes common to the substrate and thin film.

Supplementary Figure 2 shows the ω-2θ rocking curves measured at room temperature for (200) and (400) Bragg reflections of the substrate and thin film respectively for 50 nm Fe_3O_4 film on MgO substrate) The horizontal axis in the figure is shown with reference to the Bragg angle for symmetric (200) reflection of MgO substrate. From the separation between the film and substrate Bragg peaks we determine the out-of-plane lattice constant and it is found to be 0.8372 nm. The full width at half maximum for the thin film peak is found to be 0.065 degrees.

The in-plane lattice parameters of the films were determined from the asymmetric (622/311) Bragg reflections. We found that the in-plane lattice constant of Fe_3O_4 thin film (0.84236 nm) is twice that of the MgO substrate (0.4213 nm). The FWHM for the thin film peak is found to be 0.021 degrees. From the in-situ RHEED and ex-situ HRXRD characterization, we infer that the films grow pseudomorphically and maintain one-to-one registry with the MgO substrate. The unit cell volume of the film is a good indication of the film stoichiometry and is consistent with bulk magnetite suggesting that the films are stoichiometric.

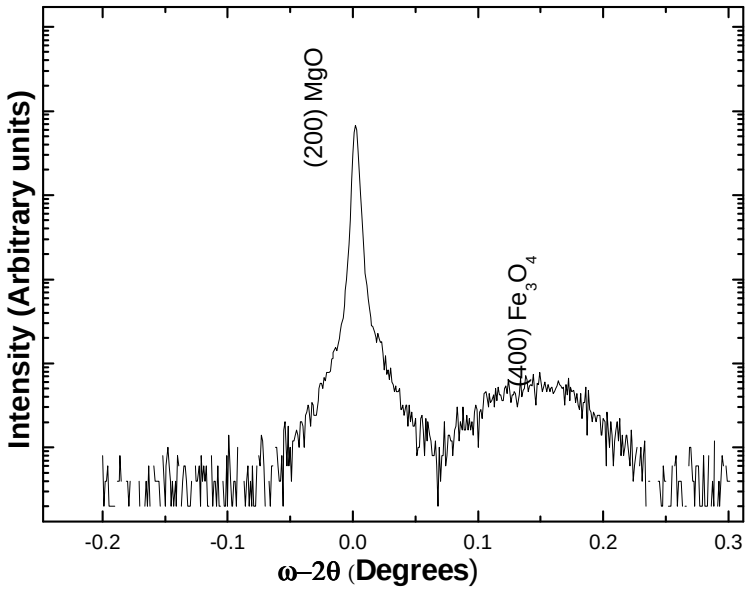

Supplementary Figure 2: The ω-2θ scans of 50nm film measured relative to the (200) Bragg reflection of MgO.

Electrical resistivity measurement of films

For electrical resistivity and magneto-resistance measurements a standard dc-four probe technique was employed. The sample was mounted on a copper block fitted onto a cold finger of the closed cycle refrigerator. Temperature of the sample stage was monitored using a GaAlAs thermometer and controlled within ±0.05 K.

Supplementary Figure 3 shows resistivity as a function of temperature in a 45nm film. Verwey transition was observed at 108 K. Since Verwey transition is very sensitive to the Fe_3O_4 film stoichiometry the observation of Verwey transition confirms that films are stoichiometric [3, 4].

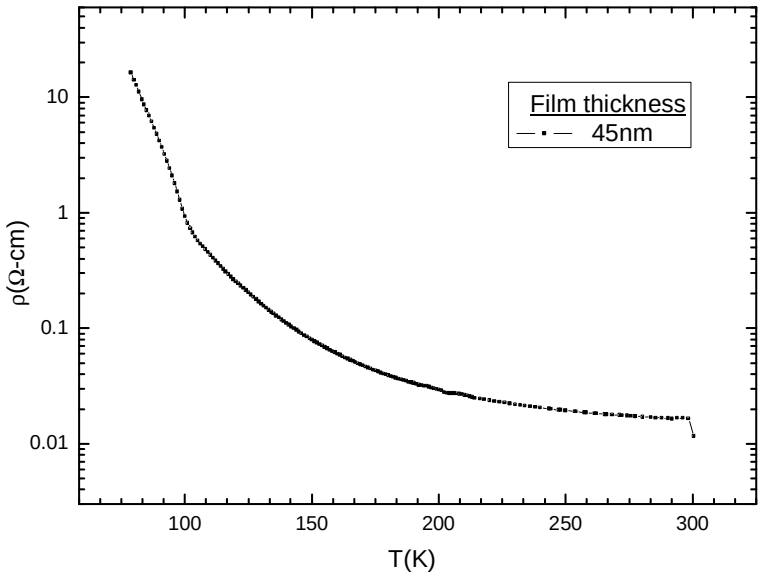

Supplementary Figure 3: Verwey transition observed for 45nm Fe_3O_4 film grown on MgO substrate under conditions identical to those used in films for devices in this work.

Magnetite nanocrystal preparation

Magnetite (Fe_3O_4) nanocrystals were synthesized[5] in a three-neck flask equipped with condenser, magnetic stirrer, thermocouple and heating mantle. In a typical run, a ground fine powder of 0.178 g FeO(OH) (2.00 mmol) was dissolved in 2.26 g oleic acid (8.00 mmol) and 5.00 g 1-octadecene and then was heated under stirring to 320 ºC and kept at this temperature for 60 minutes. Magnetite materials were completely recovered by transferring into polar (acetone) solvent to remove all the unreacted chemicals and side products, and non-polar (hexane or chloroform) solvent for redispersing and storage. No size selective precipitation was applied to these samples. Transmission electron micrographs of two nanoparticle batches used in this work are shown in Supp. Fig. 4.

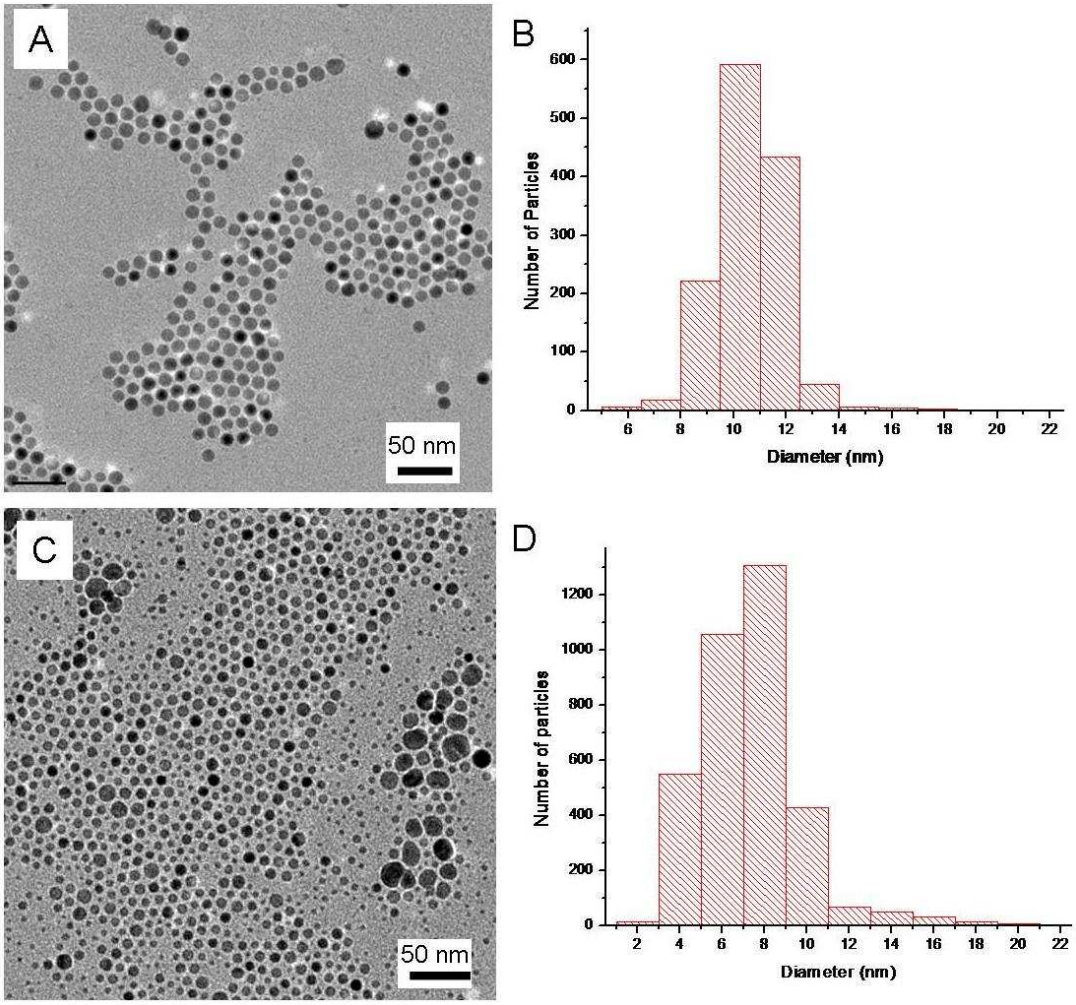

Supplementary Figure 4: Transmission Electron Micrographs (TEM) of magnetite samples and their corresponding histograms. A-B) 10.6 ± 1.3 nm magnetite nanocrystals (sample code JTM-II-75A), C-D) 7.34 ± 2.49 nm magnetite nanocrystals (sample code CTY-VI-28C-60).

Nanocrystal structural characterization

Supplementary Figure 5 shows powder XRD data taken on a precipitate prepared from batch CTY-VI-28C-60 above, performed on a Rigaku D/Max Ultima II diffractometer with Cu Kα radiation (λ=1.5406 Å and λ=1.5444 Å for Cu $K\alpha_1$ and Cu $K\alpha_2$, respectively). The powder for the XRD experiment was prepared in a two-step process. First, magnetite nanoparticles were precipitated from hexane solution by adding acetone and subsequent centrifugation at 35000 rpm. Second, the resulting oily powder – magnetite nanoparticles covered with oleic acid – was annealed at 673K in vacuum for 1 hour (as was done for the actual nanocrystal devices) to decompose and remove the oleic acid.[6] Peaks positions are compared with those (red) expected for essentially bulk magnetite[7]. The systematic shift of peak position corresponds to a deviation in lattice constant of roughly 0.4% from the bulk value. Unlabeled small peaks may indicate some small fraction of maghemite (γ-Fe_2O_3), though interpretation of XRD data for nanocrystals is complicated by the effects of strain and changes in symmetry due to interfaces and defects.[8] The magnetite/maghemite spectra are particularly challenging[9]; bulk magnetite has an extremely symmetric crystal structure (space group $Fd\bar{3}m$), while maghemite has a structure of somewhat lower symmetry (space group $P4_332$). As noted in the main text, the fact that the measured transition temperature in the nanocrystal devices is close to the Verwey temperature of bulk magnetite strongly implies that the stoichiometry of the dominant conduction path is very close to Fe_3O_4. A deviation in oxygen stoichiometry by as little as 1% suppresses T_V in bulk magnetite by ~ 40 K.[4]

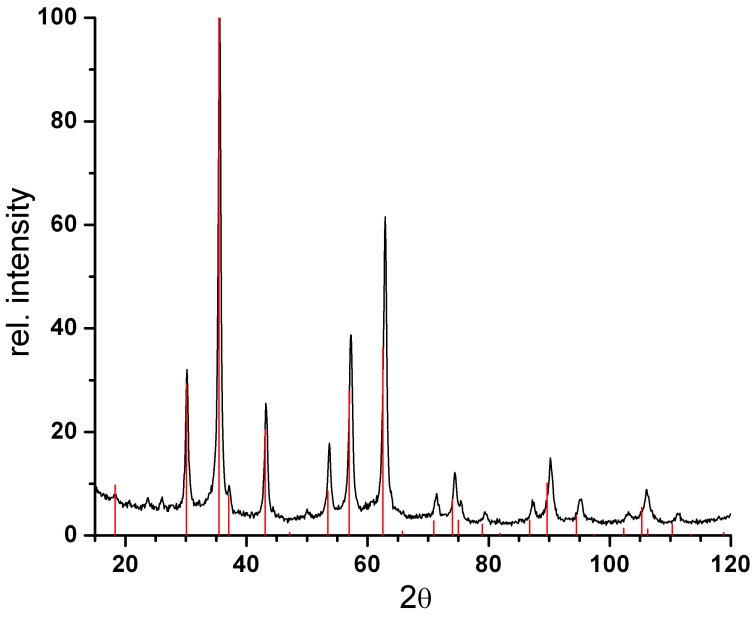

Supplementary Figure 5: Powder XRD spectrum of vacuum-annealed precipitate prepared from batch CTY-VI-28C-60. Indicated peak positions correspond to powder peaks from bulk magnetite, as identified by Fleet[7].

Example SEM images of nanocrystal devices and film devices

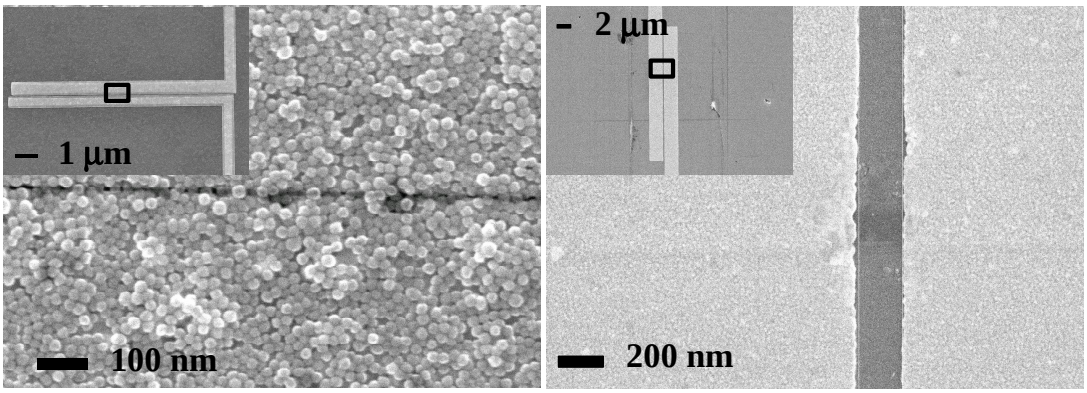

Supplementary Figure 6: Scanning electron microscope (SEM) images of magnetite nanostructures. Left: Nanocrystal-based device, showing closely spaced Au electrodes coated with 1+ monolayers of 20 nm diameter magnetite nanocrystals. The substrate in this case is degenerately doped *p*+ Si, topped by 200 nm of thermally grown SiO_2. Right: 200 nm channel length film device, showing Au electrodes patterned directly on top of magnetite (001) film 50 nm thick, on a MgO substrate.

Supplementary Figure 6 shows representative SEM images of magnetite devices after these devices have been characterized via electrical measurements. In the nanocrystal device it is not clear how many magnetite nanoparticles are participating in the electronic transport. The initial interelectrode gap is comparable to the nanoparticle diameter. In the film device there is no adhesion layer between the Au electrodes and the Fe_3O_4 film. The scaling of device resistance with electrode spacing shows that the conductance is dominated by the region between the two electrodes.

References and Notes

1. Margulies, D. T. *et al*. Anomalous moment and anisotropy behavior in Fe_3O_4 films. *Phys. Rev. B* **53**, 9175-9187 (1996).

2. Voogt, F. C. *et al*. Superparamagnetic behavior of structural domains in epitaxial ultrathin magnetite films. *Phys. Rev. B* **57**, R8107-R8110 (1998).

3. Kündig, W. & Hargrove, R. S. Electron hopping in magnetite. *Solid State Comm.* **7**, 223-227 (1969).

4. Aragón, R., Buttrey, D. J., Shepherd, J. P. & Honig, J. M. Influence of nonstoichiometry on the Verwey transition. *Phys. Rev. B* **31**, 430-436 (1985).

5. Yu, W. W., Falkner, J. C., Yavuz, C. T., & Colvin, V. L. Synthesis of monodisperse iron oxide nanocrystals by thermal decomposition of iron carboxylate salts. *Chem. Commun.* **2004**, 2306-2307 (2004).

6. Pérez-Dieste, V. *et al.* Thermal decomposition of surfactant coatings on Co and Ni nanocrystals. *Appl. Phys. Lett.* **83,** 5053-5055 (2003).

7. Fleet, M. E. The structure of magnetite: symmetry of cubic spinels. *J. Sol. State Chem.* **62**, 75-82 (1986).

8. Bawendi, M. G., Kortan, A. R., Steigerwald, M. L. & Brus, L. E. X-ray structural characterization of larger CdSe semiconductor clusters. *J. Chem. Phys.* **91**, 7282-7290 (1989).

9. Redl, F. X. *et al*., Magnetic, electronic, and structural characterization of nonstoichiometric iron oxides at the nanoscale. *J. Am. Chem. Soc*. **126**, 14583-14599 (2004).